

Persistent, rewritable frequency tuning of a nanoelectromechanical resonator using photoinduced doping

David Miller^{1,2,3}, Andrew Blaikie^{1,2,3}, and Benjamín J. Alemán^{1,2,3,4}

¹Department of Physics, University of Oregon, Eugene, Oregon

²Material Science Institute, University of Oregon, Eugene, Oregon

³Center for Optical, Molecular, and Quantum Science, University of Oregon, Eugene, Oregon

⁴Phil and Penny Knight Campus for Accelerating Scientific Impact, University of Oregon, Eugene, Oregon

Tuning the frequency of a resonant element is of vital importance in both the macroscopic world, such as when tuning a musical instrument, as well as at the nanoscale. In particular, precisely controlling the resonance frequency of isolated nanoelectromechanical resonators (NEMS) has enabled innovations such as tunable mechanical filtering and mixing¹ as well as commercial technologies such as robust timing oscillators². Much like their electronic device counterparts, the potential of NEMS grows when they are built up into large-scale arrays. Such arrays have enabled neutral-particle mass spectroscopy³ and have been proposed for ultralow-power alternatives to traditional analog electronics⁴ as well as nanomechanical information technologies like memory^{5,6}, logic⁷, and computing^{8–11}. A fundamental challenge to these applications is to precisely tune the vibrational frequency and coupling of all resonators in the array, since traditional tuning methods, like patterned electrostatic gating^{12,13} or dielectric tuning¹⁴, become intractable when devices are densely packed. Here, we demonstrate a persistent, rewritable, scalable, and high-speed frequency tuning method for graphene-based NEMS^{15–18}. Our method uses a focused laser and two shared electrical contacts to photodope^{19–22} individual resonators by simultaneously applying optical and electrostatic fields. After the

fields are removed, the trapped charge created by this process persists and applies a local electrostatic tension to the resonators, tuning their frequencies. By providing a facile means to locally address the strain of a NEMS resonator, this approach lays the groundwork for fully programmable large-scale NEMS lattices and networks^{23,24}.

Like tightening a tuning peg to tension a violin string, nanoelectromechanical resonators (NEMS) require methods to tune the resonance frequency that are persistent (*i.e.* have memory), reversible, and tunable over a large range. For large arrays, the tuning method must also be fast and scalable. While active tuning methods such as electrostatic gating^{12,13,15,18} or dielectric tuning¹⁴ are reversible and can achieve a large tuning range, they are not persistent or scalable to large arrays. Passive methods that permanently modify the NEMS structure, like mass deposition²⁵ or thermal buckling²⁶, have achieved persistent tunability. However, once set to an initial value, the resonance frequency cannot be modified in a controlled way, even to offset frequency drift. Only a few NEMS tuning approaches have combined persistence and reversibility^{27,28}, but these are limited to single devices and suffer from a combination of poor frequency resolution, a limited tuning range ($\sim 10\%$), slow speed, and limited cyclability.

In this letter, we report reversible and long-lived frequency tuning of graphene and graphene/hexagonal boron nitride (hBN) NEMS membrane resonators. Our technique uses spatially resolved photodoping^{19–22}, requiring only a focused laser and a global gate voltage V_g , to generate rewritable, trapped charges. These charges create a local potential that shifts the mechanical charge neutrality point²⁹ from its intrinsic value (near 0 V) to V_{mCNP} . The new

effective potential, $V_{eff} = V_g - V_{mCNP}$, tunes the mechanical resonance frequency, $f_0(V_{eff})$, through electrostatic tension, analogous to a standard electrostatic back-gate^{15,18} but without the need for a continuous external power supply.

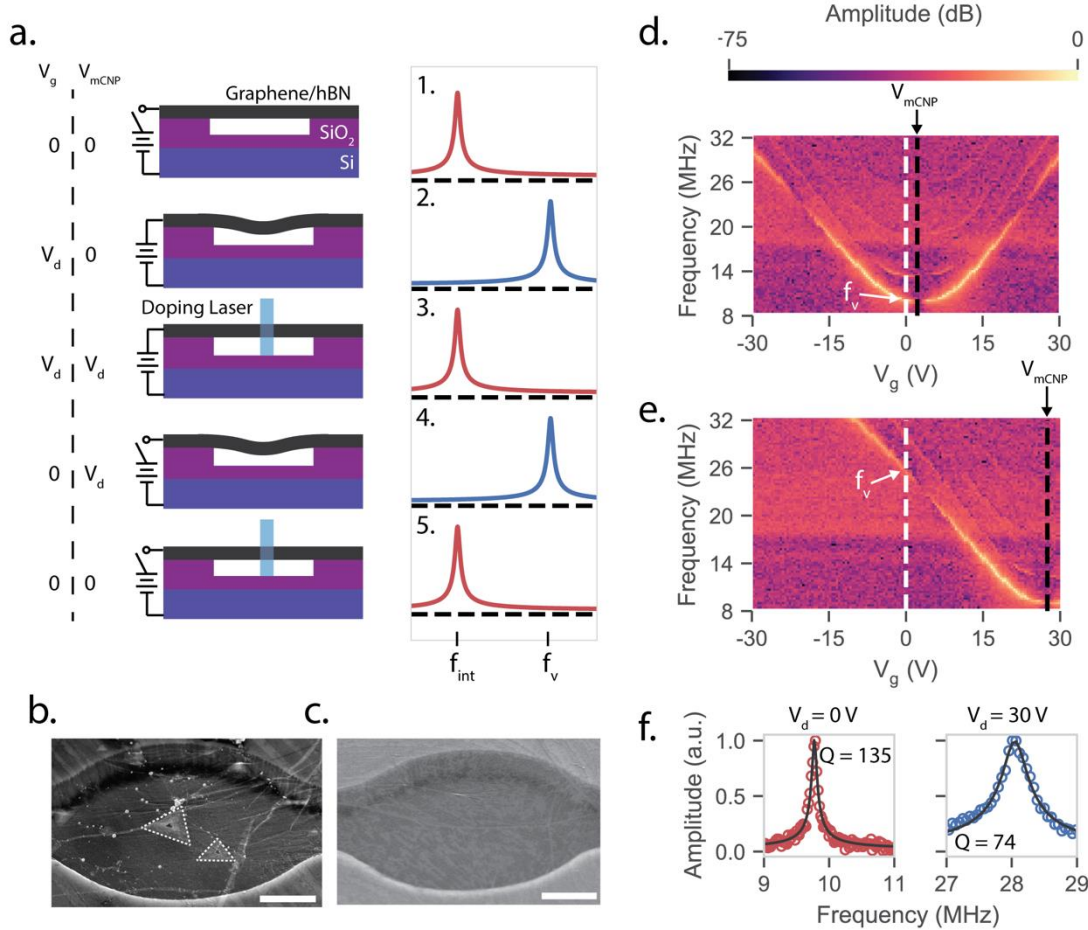


Figure 1: (a) The frequency tuning sequence. 1: Device in its intrinsic state with $V_g = 0$ V, $V_{mCNP} = 0$, and resonance frequency $f_{int} = f_0(V_{eff} = 0)$. 2: Device biased with $V_g = V_d$ and a resonance frequency of $f_0(V_d)$. 3: Photodoping the device while $V_g = V_d$ sets V_{mCNP} to V_d returns the resonance frequency to f_{int} . 4: With the gate off, the device is in its phototuned state with a resonance frequency $f_v = f_0(V_{mCNP})$. 5: Photodoping with $V_g = 0$ now returns the device to its initial configuration, with a frequency f_{int} . (b) SEM image of a 4.5 μ m gr/hBN drumhead with venting trenches on the sides. Small multilayer islands of h-BN are visible on the surface. Scale = 1 μ m. (c) SEM image of a 4 μ m graphene drumhead. Scale = 1 μ m. (d) Electrostatic tuning curves for a gr/hBN drumhead resonator phototuned to the erased state, i.e. with $V_d = 0$ V. The V_{mCNP} is initially located at ~ 1 V. (e) Electrostatic tuning curves for the same device as in (d) after phototuning with $V_d = 30$ V, with $V_{mCNP} \sim 28$ V. The overall shape of the tuning curves remains the same in all cases. (f) Resonant response with $V_{mCNP} \sim 1$ V (left, red, 9.8 MHz) and $V_{mCNP} \sim 28$ V (right, blue, 28 MHz). Between the two phototuned states, the resonance frequency shifts by $\sim 250\%$ and the Q -factor decreases from 135 to 74.

To set or change the frequency of an individual membrane through photodoping—a process we call phototuning—we apply a bias to a global back-gate (in this case, degenerately doped silicon) while focusing a laser onto the individual, suspended membrane of interest (see Figure 1a). Prior to any photodoping and assuming an initial V_{mCNP} of 0 V, the resonator will be at its intrinsic resonance frequency $f_{int} = f_0(0)$ before the laser or bias are turned on (*step 1*). Then, we set the gate voltage to a value V_d , tensioning the membrane and blue-shifting the resonance frequency (*step 2*) from f_{int} to $f_0(V_d)$. Next, with the bias still at V_d , we turn the laser on to start the charge-trapping process. This brings V_{mCNP} towards V_d , lowering V_{eff} , and red shifting the resonance frequency. Given enough laser dose, V_{mCNP} saturates at V_d and the frequency returns to f_{int} (*step 3*). After turning the laser and bias off, the frequency immediately blue-shifts to $f_0(-V_d)$ (*step 4*), which is the same as $f_0(V_d)$ due to the symmetry of $f_0(V_{eff})$. The phototuned frequency obtained after *step 4* does not require an external gate bias to maintain and is denoted $f_V = f_0(V_{mCNP})$. Steps 1-4 complete the phototuning “write” function. The frequency can be reset back to f_{int} —or “erased”—by zeroing the bias voltage ($V_g = 0$ V) and illuminating the membrane with the laser (*step 5*). We note that the description above represents the ideal case of phototuning. For most devices we study, V_{mCNP} is initially slightly offset from zero and V_{mCNP} saturates at a slightly different value than V_d , neither of these factors affect the robustness of the phototuning method.

We have phototuned the frequency of NEMS membranes made from both CVD-grown monolayer graphene and a graphene/hBN heterostructure (gr/hBN). Our devices consist of the two-dimensional sheet suspended over $\sim 4 - 5$ μm diameter circular cavities etched into SiO_2 on

degenerately doped silicon (see Figure 1a-c). A layer of SiO₂ (~300 nm thick) is left at the bottom of the cavities to prevent shorting and create potential charge traps²⁰. The devices are driven with standard electrostatic actuation techniques¹⁵ using the silicon back-gate and a Ti/Pt top contact, and measured using an interferometer operating at 633 nm^{12,16}. Photodoping is typically performed with a power-stabilized 445 nm diode laser except where noted otherwise.

The effects of phototuning are most apparent looking at the gate voltage tuning curves and frequency response spectra. We show these for a gr/hBN device in the erased state (photodoped with $V_d = 0$ V) and the tuned state (photodoped with $V_d = 30$ V), shown in Figures 1d and 1e, respectively. For both measurements, the membrane was photodoped to saturation by rastering the laser over the area of the drumhead at relatively high power (~ 1 mW/ μm^2). The fundamental mode is the easiest to resolve, but several higher order modes are also present. The curve shapes are consistent with an electrostatically biased membrane^{15,18}. In the erased state, V_{mCNP} is offset from zero by ~ 1 V, which is common and indicates the presence of static charged contaminants. With $V_d = 30$ V, V_{mCNP} saturates to ~ 28 V, where the new potential arises from charged defects in the h-BN^{19,21} and the oxide²⁰. Although V_{mCNP} differs by ~ 27 V between the two states, the gate-dependence of each mode relative to V_{mCNP} doesn't change, as seen in Figure 1d-e. Thus, apart from the V_{mCNP} shift, the phototuning process does not appear to alter the mechanical characteristics of the device in a significant way, unlike most passive tuning methods^{25,26}. The individual resonance curves corresponding to the erased and $V_d = 30$ V states are shown in Figure 1f. As V_{mCNP} changes from ~ 0 to ~ 28 V, f_V increases from ~ 9.8 MHz to ~ 28 MHz, a change of $\sim 250\%$. The Q of the 28 MHz peak ($Q = 74$) is smaller than that of the 9.8 MHz peak

($Q = 135$), just as in the case of an applied electrostatic backgate¹⁷. Although the central focus of this work is to report the phototuning effect, it also reveals that measuring or driving¹⁵ 2D NEMS with an optical probe can lead to unintended frequency drift.

To demonstrate the reversibility of f_V using phototuning, we change f_V at discrete time intervals by varying the doping potential. At the beginning of each interval, we phototune the device using a single short, high power laser pulse (~ 2 mW, 0.5 s) at a given V_d , and then continuously monitor the f_V for the remainder of the interval, ~ 600 seconds. Increasing V_d step-wise from 0 to 35 V (as seen in Figure 2a), f_V takes on fixed, stable values that increase from 7 MHz up to 45 MHz. When we decrease V_d step-wise back to 0 V, f_V returns to 7 MHz. This data clearly demonstrates that the phototuning of f_V is both reversible and bidirectional. The tuning range of f_V is large, here nearly 550%, which is an order of magnitude larger than previous hybrid tuning methods^{27,28}. For a quality factor of a typical device ($Q \sim 100$), this tuning range equals 543 resonance linewidths. In our measurements we limited the doping potential to 35 V to avoid damage to the mechanical resonators, but larger potentials up to the dielectric breakdown of the SiO_2 could be used to achieve an even higher degree of tuning.

The frequency phototuning method is persistent. This persistence is clear from the steps in Figure 2a, which show f_V is stable for at least 600 s. To assess the longer-term stability of phototuning, we write f_V a single time and then measure f_V every hour over the course of 3 days. Figure 2b plots the fractional change $\Delta f_V / f_V$ after phototuning f_V with a doping potential of 30 V. Initially,

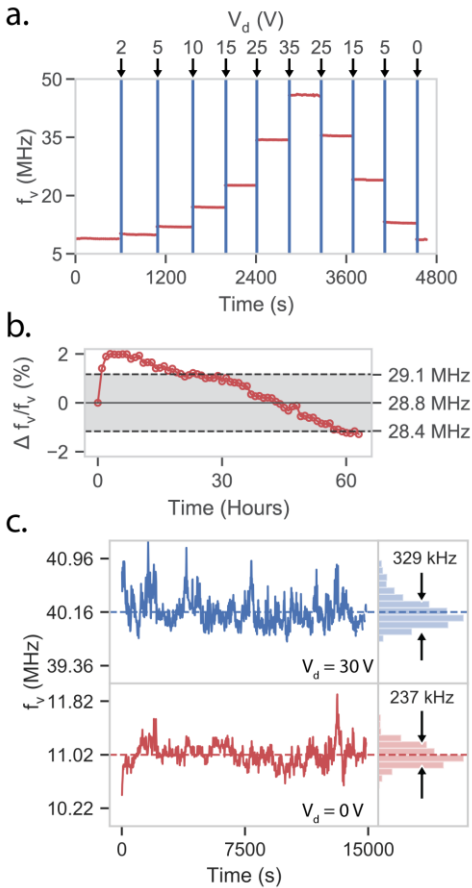


Figure 2: (a) Setting the frequency in time. A combined high-power optical pulse of $\sim 100 \mu\text{s}$ and gate voltage are applied at the times indicated by arrows. **(b)** Stability of f_V with $V_g = 0 \text{ V}$ after phototuning to 28.8 MHz. After an initial jump of 2%, the f_V decays at a rate of $\sim 0.05\%/ \text{Hour}$. The gray band shows the mechanical linewidth corresponding to a Q of 83. **(c)** Reproducibility of f_V for 919 complete cycles of phototuning with $V_d = 30 \text{ V}$ followed by erasure with $V_d = 0 \text{ V}$. The f_V value falls within a $\sim 0.2 \text{ MHz}$ band for both states.

f_V blueshifts by 2% over the course of 2 hours. After this initial detuning, the device slowly relaxes and f_V redshifts at a rate of 0.05%/hour. For reference, the mechanical linewidth for our devices is $\sim 2\%$ of the resonance frequency (shaded region of Figure 2b), so the frequency shifts by a linewidth in ~ 40 hours. This long-lived state does not require an external power supply or gate bias. Therefore, phototuning can replace patterned gate electrodes^{13,24}, even in arbitrarily large resonator arrays. To isolate the effect of the probe laser, which will cause some detuning, we set f_V and measure it once after 8 days (Supplementary Information). We still observe a small amount of detuning in addition to warping of the gate tuning spectrum. Therefore, additional sources of detuning are present and may include the rearrangement of the trapped charge in the oxide or h-BN, or strain relaxation (*e.g.* in folds and edge

clamping). Improved stability would likely be possible at cryogenic temperatures, which would reduce thermally-induced recombination of the ionized defects¹⁹. Given the time scale of the drift, feedback would be a straightforward means to stabilize the frequency.

The phototuning method can achieve a high degree of frequency tuning repeatability and can execute an indefinite number of write/erase cycles with no observable change to the mechanical properties of the NEMS device. To test repeatability and cycling performance, we erase the frequency state by phototuning with $V_d = 0$ V, then we write f_V with $V_d = 30$ V. For all writing and erasure steps, the same dose of ~ 2 mW over 0.5 s was used. Figure 2c shows the results after 919 erase/write cycles. As measured from the histogram (right of Figure 2c), the average frequencies of erased and written states are $f_{erase} = 11.02 \pm 0.12$ MHz and $f_{write} = 40.16 \pm 0.16$ MHz, which yields a writing repeatability of 99.5%. The small uncertainty in the repeatability could be inherent to the phototuning process, but could also be caused by sources of frequency noise and fluctuations common to 2D NEMS, such as adsorbates, heating, and unwrinkling¹², or fluctuations in the power of doping laser. The large frequency separation of the written and erased states in Figure 2a and Figure 2c could easily allow a discrete binary logic state^{5,11} or, given the measured error of 160 KHz, over 150 discrete and well-defined logic states.

The temporal rate of the phototuning method is exceptionally fast. The phototuning rate can be inferred from the time-dependence of either f_V or V_{mCNP} during the phototuning process (see Methods). Figure 3a shows a plot of $V_{mCNP}(t)$ (blue, upper) and $f_V(t)$ (orange, lower) for $V_d = 9$ V, and $P \sim 530$ μ W with a 445 nm laser. Both V_{mCNP} and f_V approach steady state saturation values within ~ 10 ms. As noted earlier, we find that V_{mCNP} does not saturate exactly to V_d , but each device has a small but consistent offset, which we denote δV_{mCNP} . To obtain the doping rate, we approximate $V_{mCNP}(t)$ with a saturation function of the form,

$$(1) \quad V_{mCNP}(t) = \Delta V(1 - e^{-\alpha t}) + V_0$$

Where $\Delta V \approx V_d - V_0 + \delta V_{mCNP}$, V_0 is fixed at the initial V_{mCNP} , and α is the doping rate, which depends on the laser's power, wavelength, and position^{22,30}. Prior to each rate measurement, the device is photodoped at high power with $V_d = 0$ V, which initializes V_0 to δV_{mCNP} . The black trace in the upper plot of Figure 3a is the fit for $V_{mCNP}(t)$ using Eq. 1, with fit parameters $\Delta V = 8.94$ V and $\alpha = 124$ s⁻¹. In this model, the instantaneous doping rate is $\left| \frac{dV_{mCNP}(0)}{dt} \right| = |\Delta V|\alpha$, and the frequency tuning rate is $R_f \equiv \left| \frac{dV_{mCNP}(0)}{dt} \right| \frac{df_0}{dV_g} = \alpha |\Delta V| \frac{df_0}{dV_g}$, where $\frac{df_0}{dV_g}$ is the slope of the photodoped gate voltage tuning curve at $V_g = 0$ V (*i.e.* at f_V). With $|V_{mCNP}| \sim 8$ V, $\frac{df}{dV_g}$ is between 0.2 – 1.5 MHz/V (Supplementary Information), which with $|\Delta V| = 1$ V gives a range of $R_f \sim 24 - 181$ MHz/s. $\frac{df_0}{dV_g}$ is determined by the device geometry¹⁸ and strain, and could be increased by using small area devices or shallower cavities. We note that R_f characterizes the change in the steady-state f_V for a particular dose, not the dynamic change in f_V , which is limited by the RC time constant of the device (~ 1 μ s). Still, the frequency tuning rate of phototuning is exceptionally fast; for example, with a moderate bias voltage of ~ 10 V and optical power of 1 mW, it is possible to tune a resonator by its full linewidth in ~ 100 μ s (10^4 resonators per second) or to enable feedback control with a bandwidth exceeding 10 kHz. Even faster tuning rates should be possible by increasing the laser power further, since graphene resonators are stable up to at least 1200 K³¹.

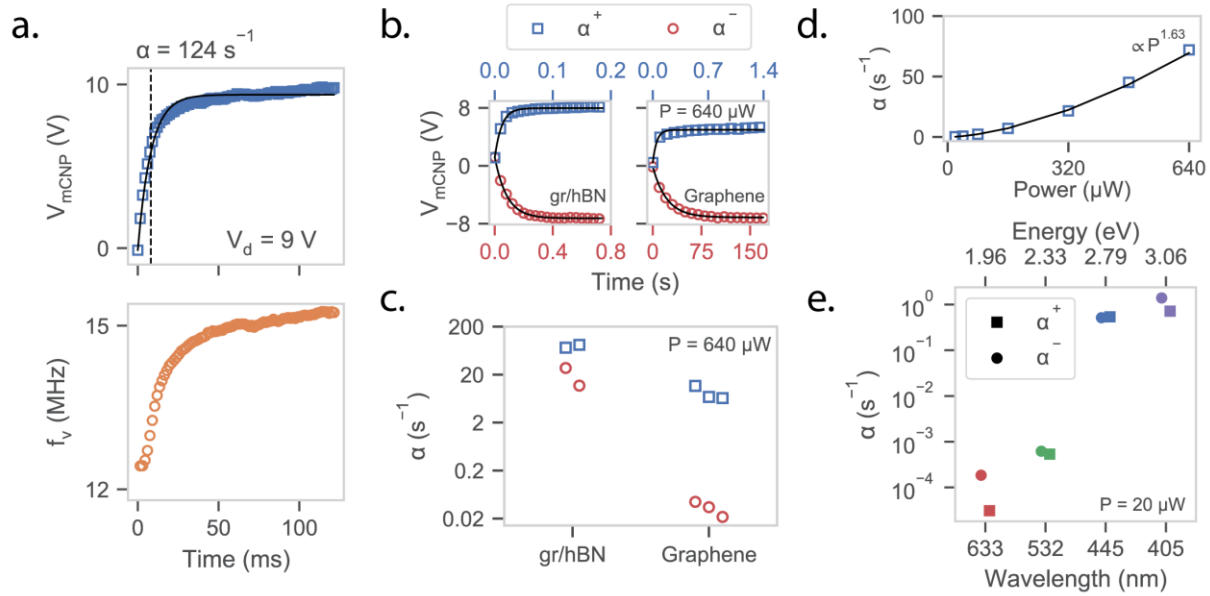


Figure 3: Measurements of the photodoping rates. The laser wavelength is 445 nm except in e. **(a)** Top: Example of a single photodoping curve with $V_d = 9$ V. The black line is an exponential fit to the data with $\alpha = 124$ s $^{-1}$. Bottom: Same data for f_v . **(b)** Photodoping curves for $\Delta V > 0$ in blue (α^+ branch) and $\Delta V < 0$ in red (α^- branch) for a gr/hBN device and a graphene-only device. The laser power is 640 μ W and $V_d = \pm 8$ V for all the measurements. **(c)** Doping rates for both α^+ (blue squares) and α^- (red circles) for 640 μ W, 445 nm irradiation for two gr/hBN and three graphene devices. For the α^+ branch of the graphene devices, which don't saturate close to V_d , we take the initial slope of $V_{mCNP}(t)$ and divide by V_d to obtain α . **(d)** Laser-power dependent doping rate for the α^+ branch of one of the gr/hBN devices in c. The black line is a fit to the function $\alpha = \alpha_0 P^\gamma$, with $\gamma = 1.63$. **(e)** Photodoping rates of a gr/hBN device for both the α^+ (squares) and α^- (circles) branches. Data was collected using 405 nm, 445 nm, 532 nm, and 633 nm illumination all at 20 μ W. The photodoping rate increases by a factor of 10^4 from 633 nm to 405 nm illumination. For the 532 nm and 633 nm laser illumination, we use the same linearized doping rate defined in c.

The photodoping rate depends on the device material (graphene vs. gr/hBN), the polarity of ΔV , and the optical power. We measure α with optical power ranging from 20 – 2540 μ W (See SI for full power range) with a blue doping laser (445 nm) and set $V_d = \pm 8$ V. The results for two graphene/hBN and three graphene-only devices (Figure 3b-c) show several features. First, the photodoping rate depends on whether $\Delta V < 0$ (α^- branch) or $\Delta V > 0$ (α^+ branch) (Figure 3b). For all devices, $\alpha^+ > \alpha^-$, but the difference can vary greatly. For the gr/hBN devices, $\alpha^+ \sim 2\alpha^-$, while for graphene-only devices $\alpha^+ \sim 10^3 \times \alpha^-$ (Figure 3c). Second, while δV_{mCNP} is less than

15% of V_d for both branches of the gr/hBN devices, this is only true for the slower α^- branch of the graphene devices. For the α^+ branch of the graphene device, δV_{mCNP} can be as large as $\sim 50\%$ of V_d (Figure 3b). Third, both α branches follow a non-linear dependence on the power, $\alpha(P) = \alpha_0 P^\gamma$, where γ is between 1.4 – 1.6 for gr/hBN devices and 1.2 – 1.7 for the graphene devices (see Supplementary Information). Figure 3d illustrates an example of $\alpha(P)$ for the α^+ branch of a gr/hBN device with laser power increasing from 20 – 640 μW , where the black line is a fit with $\gamma = 1.63$. The non-linear dependence on the power shows that the phototuning effect is not purely determined by delivered energy, but is also potentially due to local laser-induced heating of the suspended 2D sheets¹⁶, which would lower the energy barrier between the donors (acceptors) and the conduction (valence) bands. Lastly, α for gr/hBN devices is greater than for graphene-only devices, regardless of branch, although the difference is significantly larger for the α^- branch, which can differ by a factor of $10^2 - 10^3$ (Figure 3c). The differences in the rates and the value of ΔV between the gr/hBN and graphene-only devices suggests that the gr/hBN heterostructure has a higher density of ionizable dopants and/or a lower dopant ionization energy, consistent with previous reports of electronic photodoping^{19,20}.

The phototuning rate is greater for shorter wavelength light. To characterize the wavelength dependence of α , we measure α using four different laser wavelengths (633, 532, 445, 405 nm) with an optical power of 20 μW and $|V_d| = 8$ V. The results (Figure 3e) show that shorter wavelength, higher energy illumination leads to much faster phototuning. Compared to 633 nm light ($\alpha^+ = 1.8 \times 10^{-4} \text{ s}^{-1}$ and $\alpha^- = 3.1 \times 10^{-5} \text{ s}^{-1}$), α for 405 nm light ($\alpha^+ = 1.3 \text{ s}^{-1}$ and $\alpha^- = 0.72 \text{ s}^{-1}$) is larger by a factor of $\sim 10^4$. The rate increase also appears to be saturating near 3 eV.

The enhanced phototuning at shorter wavelengths agrees with previous photodoping studies in h-BN as well as SiO₂^{20,21,32}. The wavelength dependence of α is advantageous for nanomechanics experiments, as it allows selection of a long-wavelength laser for transduction, which has a negligible phototuning effect, and a short-wavelength laser for phototuning. We note that higher photon energies likely also induce photodoping, which could explain the frequency shifts seen in γ -ray irradiated 2D sheets³³.

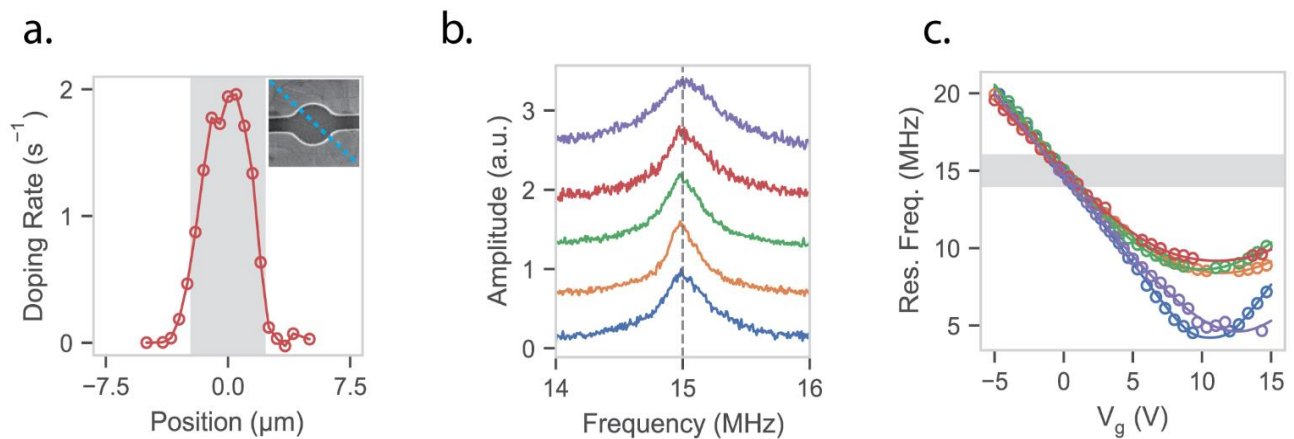


Figure 4: (a) Photodoping rate as the doping laser is scanned across a gr/hBN drumhead. The scan line is indicated in the SEM image inset. The doping rate reaches a maximum at the center of the drum and rapidly falls off as it is swept away. The gray band indicates the spatial extent of the device. (b) Resonant response for five different Gr/hBN devices displaying alignment of f_V to 15 MHz of less than 0.2%. The alignment is achieved with no external electrical gate bias. (c) Electrostatic tuning curves for the fundamental mode of the five devices from Figure 4b (the data color corresponds to each device) after being simultaneously phototuned to $f_V = 15$ MHz. The gray horizontal band corresponds to the 14-16 MHz plot range of b.

Many applications in NEMS circuits and lattices require precise, programmable frequency and strain tuning of individual resonators within large arrays on a single chip^{13,24}. To demonstrate this capability with phototuning, we first show that the effect is localized to the laser spot. Figure 4a shows the doping rate at 20 μW measured at different locations on the membrane. The device begins to photodope only when the gaussian spot of the laser overlaps with the area of the membrane. We use the dilation of the spatial doping rate profile relative to the device diameter

(greyed region in Figure 4a) to infer a spatial resolution of $\sim 1 \mu\text{m}$, which is approximately the size of the laser spot. Next, we align the frequencies of five different Gr/hBN devices to within 30 kHz (or 0.2%) of $f_V = 15 \text{ MHz}$, as shown in the Figure 4b amplitude spectra, achieving a tuning precision within $\sim 5\%$ of a resonance linewidth. The resonance frequency gate curves for each device are shown in Figure 4c. While the curves intersect at $V_g = 0 \text{ V}$, which defines f_V , the values of V_{mCNP} and the general curve shape vary considerably. This demonstrates that phototuning is largely insensitive to variations between individual resonators and is thus a robust frequency tuning method.

In conclusion, we have demonstrated a fast, reversible, persistent, and scalable frequency tuning method based on deterministic charge trapping, which allows for optical “etch-a-sketch” patterning of strain in 2D NEMS arrays. Our phototuning technique eliminates the need for complex, lithographically defined gate electrodes used to electrostatically strain and frequency tune NEMS resonators. When applied to large NEMS lattices, this approach could enable reprogrammable phononic crystals and waveguides^{23,24}, or more exotic applications such as neuromorphic computing¹⁰ or the simulation of complex networks³⁴.

Acknowledgments

We acknowledge the facilities and staff from the Center for Advanced Materials in Oregon (CAMCOR), and the use of the University of Oregon’s Rapid Materials Prototyping facility, funded by the Murdock Charitable Trust. We thank Joshua Ziegler, Rudy Resch, and Kara Zappitelli for

scientific discussions and feedback related to this work. This work was supported by the University of Oregon and the National Science Foundation (NSF) under grant No. DMR-1532225.

Author Contributions

DM and BA conceived and designed the experiments. DM and AB fabricated the NEMS devices. DM designed and built optical measurement apparatus and performed the experiments with assistance from AB. DM analyzed the data. DM and BA wrote the manuscript, and AB provided comments on the manuscript. BA supervised the work.

Methods

Fabrication of 2D drumheads. 4.5 μm diameter gr/h-BN mechanical drumhead resonators were fabricated by transferring the 2D sheets over an array of cavities etched into 1 μm wet thermal oxide^{35,36} grown on degenerately doped silicon wafers (University Wafer). The cavities were fabricated using direct-write optical lithography and CHF_3 based reactive ion etching. A ~ 300 nm layer of oxide was left at the bottom of the cavity to act as a charge trapping layer and to prevent shorting. Ti/Pt electrodes were defined by lithography and deposited by thermal evaporation.

To prepare the 2D sheets for transfer, a relatively thick layer (~ 3 μm) of PMMA A11 was spun onto CVD grown single-layer h-BN on Cu foil (Graphene Supermarket) and then a polyamide scaffold with a central hole removed was then placed on the PMMA/hBN/Cu stack. The stack was placed in a bath of Ammonium Persulphate to etch the Cu and then rinsed in deionized water and dried in air. The polyamide/PMMA/hBN was placed on top of CVD graphene grown on Cu foil

(Graphenea) and baked at 180 °C for 30 minutes to adhere the hBN and the graphene³⁶. The etching, rinsing, and drying was repeated leaving a freestanding film of PMMA/hBN/Graphene supported by the polyamide scaffold. To transfer the 2D sheets to the cavity substrates, the PMMA/hBN/Graphene stack was then placed graphene-side-down on top of the pre-patterned cavities and adhered at 155 °C overnight (~15 hours). After removing the polyamide scaffold, the PMMA was removed in flowing Ar/H₂ at 400 °C. The graphene sheet contacts the electrodes from above, resulting in a simultaneous electrical connection to all devices. Graphene-only devices were fabricated in a similar fashion with both an in-house and a commercial transfer process performed by Graphenea.

Measurement of mechanical motion. Device motion was measured using optical interferometry, as described previously¹⁶. A 633 nm HeNe laser was focused onto the devices (held at room temperature at 10⁻⁶ torr) using a 40 ×, 0.6 NA objective. The reflected light was detected using a high-sensitivity photodiode (Thorlabs APD 130A) and the voltage signal was demodulated using a Zurich Instruments HFLI2 Lock-In amplifier. The incident laser was scanned with a two-axis galvometer and passed through an optical relay system in order to image the mode shape and to maximize transduction sensitivity. We used low laser power (~1 – 10 μW) to avoid unwanted photodoping by the 633 nm probe laser.

Photodoping. A separate laser (405 nm, 445 nm, or 532 nm) was used for photodoping. The doping laser was coupled into the beam-path using a dichroic mirror and focused onto the sample using the same 40 ×, 0.6 NA objective lens. A separate two-axis galvometer was used to position

the doping laser at the center of the drumheads. The laser power for each color was calibrated using a power meter (Thorlabs 120VC) and maintained using PID control. For dynamic measurements of V_{mCNP} , an acousto-optic modulator (AA-Optoelectronics MT350-A0.12-VIS) was used to supply a well-defined pulse of the doping laser with pulse-widths down to ~ 10 ns. Prior to all measurements, the doping laser was scanned across the device with $V_d = 0$ V to guarantee a uniformly-doped initial erased state.

Measurement of the CNP. Measurement of the mechanical charge neutrality point (V_{mCNP}) has typically been accomplished in previous work by fitting the full frequency tuning curves (such as those shown in Figure 1d-e), but this approach is too slow for a dynamic measurement of V_{mCNP} . To overcome this, we use a mechanical feedback approach, similar to Kelvin Force Probe Microscopy³⁷, to rapidly measure V_{mCNP} . The electrostatic force felt by the membrane is:

$$F \approx \frac{1}{2} \frac{dC_g}{dx} (V_g - V_{mCNP})^2 + V_{AC} \frac{dC_g}{dx} (V_g - V_{mCNP}) \cos(2\pi ft + \theta)$$

where the first term leads to frequency tuning and the second to electrostatic driving. We use the off-resonant behavior of the second term to infer V_{mCNP} . For low frequencies below both the RC time constant of the electromechanical circuit (~ 1 μ s) and the mechanical resonance frequency (~ 0.1 μ s), the phase θ will vanish. In this regime, the X-quadrature (X_{quad}) amplitude measured by the lock-in amplifier is proportional to $(V_g - V_{mCNP})$, which vanishes when $V_g = V_{mCNP}$. Thus to measure V_{mCNP} , we feedback on X_{quad} with a set point voltage $X_{quad} = 0$ V and use V_g as the output variable. The value of V_g that makes X_{quad} vanish is also V_{mCNP} .

For the dynamic measurements such as those shown in Figure 3, our protocol is as follows. First, we set the drive frequency to $f = 100$ kHz, which is well below the mechanical

resonance frequencies of ~ 10 MHz, and turn on the mechanical feedback. After a brief stabilization period, V_g is measured 10 times with the average value taken as V_{mCNP} . V_g is then fixed at V_d and a photodoping optical pulse with a predetermined width (from as low as a few milliseconds to several seconds) is applied to the device. This process is repeated until V_{mCNP} approaches V_d with both the laser power and pulse time determining the total length of the measurement, which can take several minutes depending on the resolution.

References:

1. Rhoads, J. F., Shaw, S. W., Turner, K. L. & Baskaran, R. Tunable Microelectromechanical Filters that Exploit Parametric Resonance. *J. Vib. Acoust.* **127**, 423 (2005).
2. van Beek, J. T. M. & Puers, R. A review of MEMS oscillators for frequency reference and timing applications. *J. Micromechanics Microengineering* **22**, 013001 (2012).
3. Dominguez-Medina, S. *et al.* Neutral mass spectrometry of virus capsids above 100 megadaltons with nanomechanical resonators. *Science* **362**, 918–922 (2018).
4. Ekinci, K. L. & Roukes, M. L. Nanoelectromechanical systems. *Rev. Sci. Instrum.* **76**, 061101 (2005).
5. Yao, A. & Hikiyara, T. Logic-memory device of a mechanical resonator. *Appl. Phys. Lett.* **105**, 123104 (2014).
6. Rueckes, T. Carbon Nanotube-Based Nonvolatile Random Access Memory for Molecular Computing. *Science* **289**, 94–97 (2000).
7. Masmanidis, S. C. *et al.* Multifunctional Nanomechanical Systems via Tunably Coupled Piezoelectric Actuation. *Science* **317**, 780–783 (2007).
8. Hafiz, M. A. A., Kosuru, L. & Younis, M. I. Towards electromechanical computation: An alternative approach to realize complex logic circuits. *J. Appl. Phys.* **120**, (2016).
9. Roukes, M. L. Mechanical computation, redux? in *IEDM Technical Digest. IEEE International Electron Devices Meeting, 2004.* 539–542 (IEEE, 2004). doi:10.1109/IEDM.2004.1419213
10. Hoppensteadt, F. C. & Izhikevich, E. M. Synchronization of MEMS resonators and mechanical neurocomputing. *IEEE Trans. Circuits Syst. I Fundam. Theory Appl.* **48**, 133–138 (2001).
11. Mahboob, I. & Yamaguchi, H. Bit storage and bit flip operations in an electromechanical oscillator. *Nat. Nanotechnol.* **3**, 275–279 (2008).
12. De Alba, R. *et al.* Tunable phonon-cavity coupling in graphene membranes. *Nat. Nanotechnol.* **11**, 741–746 (2016).
13. Cha, J. & Daraio, C. Electrical tuning of elastic wave propagation in nanomechanical

- lattices at MHz frequencies. *Nat. Nanotechnol.* **13**, 1016–1020 (2018).
14. Unterreithmeier, Q. P., Weig, E. M. & Kotthaus, J. P. Universal transduction scheme for nanomechanical systems based on dielectric forces. *Nature* **458**, 1001–1004 (2009).
 15. Bunch, J. S. *et al.* Electromechanical Resonators from Graphene Sheets. *Science* **315**, 490–493 (2007).
 16. Davidovikj, D. *et al.* Visualizing the Motion of Graphene Nanodrums. *Nano Lett.* **16**, 2768–2773 (2016).
 17. Song, X. *et al.* Stamp transferred suspended graphene mechanical resonators for radio frequency electrical readout. *Nano Lett.* **12**, 198–202 (2012).
 18. Chen, C. *et al.* Performance of monolayer graphene nanomechanical resonators with electrical readout. *Nat. Nanotechnol.* **4**, 861–867 (2009).
 19. Ju, L. *et al.* Photoinduced doping in heterostructures of graphene and boron nitride. *Nat. Nanotechnol.* **9**, 348–352 (2014).
 20. Kim, Y. D. *et al.* Focused-Laser-Enabled p–n Junctions in Graphene Field-Effect Transistors. *ACS Nano* **7**, 5850–5857 (2013).
 21. Choi, H. H. *et al.* Photoelectric Memory Effect in Graphene Heterostructure Field-Effect Transistors Based on Dual Dielectrics. *ACS Photonics* **5**, 329–336 (2018).
 22. Neumann, C. *et al.* Spatial Control of Laser-Induced Doping Profiles in Graphene on Hexagonal Boron Nitride. *ACS Appl. Mater. Interfaces* **8**, 9377–9383 (2016).
 23. Cha, J., Kim, K. W. & Daraio, C. Experimental realization of on-chip topological nanoelectromechanical metamaterials. *Nature* **564**, 229–233 (2018).
 24. Hatanaka, D., Bachtold, A. & Yamaguchi, H. Electrostatically Induced Phononic Crystal. *Phys. Rev. Appl.* **11**, 024024 (2019).
 25. Enderling, S. *et al.* Characterization of frequency tuning using focused ion beam platinum deposition. *J. Micromechanics Microengineering* **17**, 213–219 (2007).
 26. Merced, E., Cabrera, R., Dávila, N., Fernández, F. E. & Sepúlveda, N. A micro-mechanical resonator with programmable frequency capability. *Smart Mater. Struct.* **21**, (2012).
 27. Kim, K., Jensen, K. & Zettl, A. Tuning nanoelectromechanical resonators with mass migration. *Nano Lett.* **9**, 3209–3213 (2009).
 28. Chang, J. *et al.* Synthesis and bidirectional frequency tuning of cantilever-shape nano resonators using a focused ion beam. *ACS Appl. Mater. Interfaces* **5**, 9684–9690 (2013).
 29. Will, M. *et al.* High Quality Factor Graphene-Based Two-Dimensional Heterostructure Mechanical Resonator. *Nano Lett.* **17**, 5950–5955 (2017).
 30. Velasco, J. *et al.* Nanoscale Control of Rewriteable Doping Patterns in Pristine Graphene/Boron Nitride Heterostructures. *Nano Lett.* **16**, 1620–1625 (2016).
 31. Ye, F., Lee, J. & Feng, P. X.-L. Electrothermally Tunable Graphene Resonators Operating at Very High Temperature up to 1200 K. *Nano Lett.* **18**, 1678–1685 (2018).
 32. Ju, L. *et al.* Photoinduced doping in heterostructures of graphene and boron nitride. *Nat. Nanotechnol.* **9**, (2014).
 33. Lee, J., Krupcale, M. J. & Feng, P. X. L. Effects of γ -ray radiation on two-dimensional molybdenum disulfide (MoS₂) nanomechanical resonators. *Appl. Phys. Lett.* **108**, (2016).
 34. Matheny, M. H. *et al.* Exotic states in a simple network of nanoelectromechanical oscillators. *Science* **363**, eaav7932 (2019).

